
Exact Muffin-tin Orbitals Method

In order to reduce the very expensive computational effort of full-potential methods, often a compromise has been made between the accuracy and efficiency, and methods based on approximate single-electron potentials have been developed. The most widely used approach is based on the physically transparent *Muffin-Tin* (MT) approximation. Within this approximation, the effective potential is represented by non-overlapping spherically symmetric potentials around the atomic nuclei and a constant potential in the interstitial region. Although the mathematical formulation of the MT approach is very elegant, it gives a rather poor representation of the exact potential. The so called *Atomic Sphere Approximation* (ASA) [39] substitutes the space by overlapping spherical cells. The total volume of the ASA spheres is equal to the volume of the real space, and thus the region between spheres is completely removed. Because of the large potential spheres, the ASA brings a real improvement to the MT approximation. However, most of the conventional methods based on the ASA potential use a similar approximation for the Schrödinger and Poisson equations [43]. Therefore, with these methods, reasonably accurate results could only be obtained for close-packed systems. In order to increase the accuracy and extend the ASA methods to open systems, different corrections had to be included [39, 40, 44, 45, 48, 50].

In the 1990s, a breakthrough was made by Andersen and co-workers by developing the *Exact Muffin-Tin Orbitals* (EMTO) theory [46, 84, 85, 86]. This theory is an improved screened Korringa–Kohn–Rostoker method [38, 42], in that large overlapping potential spheres can be used for an accurate representation of the exact single-electron potential [84]. The single-electron states are calculated exactly, while the potential can include certain shape approximations, if required. By separating the approaches used for the single-electron states and for the potential, the accuracy can be sustained at a level comparable to that of the full-potential techniques without detracting significantly from the efficiency. In this chapter, we shall review the EMTO theory and introduce a self-consistent implementation of it within the *Spherical Cell Approximation* for the muffin-tin potential.

2.1 The Exact Muffin-tin Orbitals Formalism

The self-consistent solution of the Kohn–Sham equations (1.3), (1.4) and (1.7) involves two main steps. First, the solution of Equation (1.3) for the effective potential (1.4), and second, the solution of the Poisson equation¹ for the total charge density. In this section, we explicate the first problem within the EMTO formalism.

2.1.1 Optimized Overlapping Muffin-tin Wells

Within the overlapping muffin-tin approximation, the effective single-electron potential in Equation (1.4) is approximated by spherical potential wells $v_R(r_R) - v_0$ centered on lattice sites R plus a constant potential v_0 , *viz.*

$$v(\mathbf{r}) \approx v_{mt}(\mathbf{r}) \equiv v_0 + \sum_R [v_R(r_R) - v_0]. \quad (2.1)$$

By definition, $v_R(r_R)$ becomes equal to v_0 outside the potential sphere of radius s_R . For simplicity, here and in the following, we suppress the density dependence of the potential. For the vector coordinate, we use the notation $\mathbf{r}_R \equiv r_R \hat{r}_R = \mathbf{r} - \mathbf{R}$, where r_R is the modulus of \mathbf{r}_R , and omit the vector notation for index R .

For fixed potential spheres, the spherical and the constant potentials from the right hand side of Equation (2.1) are determined by optimizing the mean of the squared deviation between $v_{mt}(\mathbf{r})$ and $v(\mathbf{r})$, *i.e.* minimizing the

$$F_v[\{v_R\}, v_0] \equiv \int_{\Omega} \left\{ v(\mathbf{r}) - v_0 - \sum_R [v_R(r_R) - v_0] \right\}^2 d\mathbf{r} \quad (2.2)$$

functional [47]. Here Ω is a region where the potential optimization is performed, *e.g.*, the unit cell. Since F_v is a functional of the spherical potentials, the minimum condition is expressed as

$$\int_{\Omega} \delta v_R(\mathbf{r}) \frac{\delta F_v[\{v_R\}, v_0]}{\delta v_R(\mathbf{r})} d\mathbf{r} = 0 \quad \text{for any } R, \quad (2.3)$$

where $\delta/\delta v_R(\mathbf{r})$ stands for the functional derivative, and

$$\frac{\partial F_v[\{v_R\}, v_0]}{\partial v_0} = 0. \quad (2.4)$$

The solution of these integro-differential equations gives the optimal $v_R(r_R)$ and v_0 , and leads to the so called *optimized overlapping muffin-tin* (OOMT) potential. The reader is referred to Andersen *et al.* [47] for further details about the potential optimization.

¹ The Hartree potential [87] can be found either by direct integration or as the solution of the Poisson equation $\nabla^2 v_H(\mathbf{r}) = -8\pi n(\mathbf{r})$.

In the case of non-overlapping muffin-tins, Equations (2.3) and (2.4) reduce to the spherical average of the full-potential within the potential sphere, *i.e.*

$$v_R(r_R) = \frac{1}{4\pi} \int v(\mathbf{r}) d\hat{r}, \quad \text{for } r_R \leq s_R, \quad (2.5)$$

and to the space average of the full-potential within the s -interstitial region², *i.e.*

$$v_0 = \frac{1}{\Omega_{\mathcal{I}^s}} \int_{\mathcal{I}^s} v(\mathbf{r}) d\mathbf{r}, \quad (2.6)$$

where \mathcal{I}^s denotes the s -interstitial region and $\Omega_{\mathcal{I}^s} = \Omega - \sum_R \frac{4\pi s_R^3}{3}$ is the volume of the s -interstitial. Note that Equation (2.6) gives the well-known muffin-tin zero.

The overlap between potential spheres may be described in terms of the linear overlap. The linear overlap between two spheres is defined as the relative difference between the sum of the sphere radii and the distance between them, *i.e.*,

$$\omega_{RR'} \equiv \frac{s_R + s_{R'}}{|\mathbf{R} - \mathbf{R}'|} - 1. \quad (2.7)$$

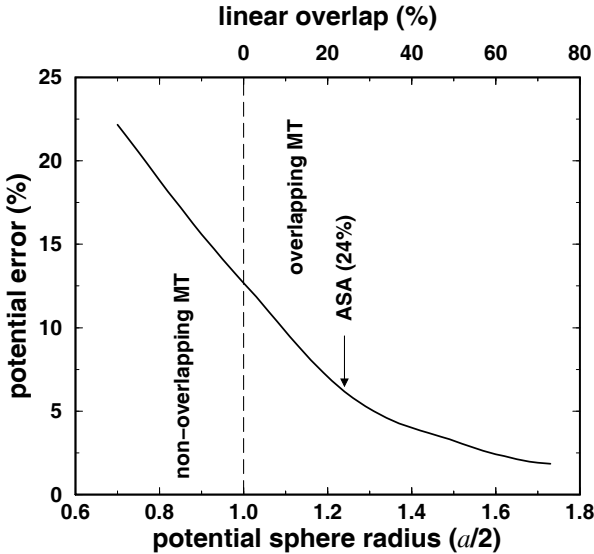


Fig. 2.1. Optimized overlapping muffin-tin potential approximation to the cosine potential in a simple cubic lattice. The radius corresponding to inscribed sphere ($s^i = a/2$) is marked by a vertical line.

² The interstitial region is the space outside of the potential spheres.

In a monoatomic system, the inscribed sphere is defined as the largest non-overlapping sphere. The radius of this sphere is $s_R^i = \min_{R'} |\mathbf{R} - \mathbf{R}'|/2$. The linear overlap is set to zero for potential spheres with radii $s_R \leq s_R^i$. Obviously, in polyatomic crystals, the inscribed sphere depends upon the convention used to divide the space into units around the lattice sites.

In the following, using a simple model potential, we demonstrate how the full-potential can be represented by overlapping muffin-tins. We model a general three dimensional full-potential by a cosine potential in a simple cubic lattice with lattice constant a . Choosing the reference level in the corner of the Wigner–Seitz cell, *i.e.* in $(a/2, a/2, a/2)$, the cosine potential has the form

$$v_c(\mathbf{r}) = -\cos\left(\frac{2\pi}{a}x\right) - \cos\left(\frac{2\pi}{a}y\right) - \cos\left(\frac{2\pi}{a}z\right) - 3, \quad (2.8)$$

where x, y, z are the Cartesian coordinates for \mathbf{r} . For this potential, we solve Equations (2.3) and (2.4), and the v_0 and $v_R(r_R)$ obtained are used to construct the optimized overlapping muffin-tin potential approximation for $v_c(\mathbf{r})$.

The integrated local deviation between $v_c(\mathbf{r})$ and its OOMT approximation is plotted in Figure 2.1 as a function of the potential sphere radius s . Results are shown from $s = 0.7s^i$ to $s = 1.7s^i$, where $s^i = a/2$ is the radius of the inscribed sphere. This interval corresponds to linear overlaps $\omega_{RR'}$ ranging from -30% to $+70\%$, as indicated at the top of the figure. We observe that the error in the muffin-tin potential decreases continuously with increasing potential sphere radius. Around linear overlaps corresponding to the ASA ($\sim 24\%$), the error falls to below half of the error observed for touching, *i.e.*, non-overlapping spheres. From these results one can clearly see that the accuracy of the overlapping muffin-tin approximation to the full-potential can be improved substantially by increasing the overlap between the potential spheres.

2.1.2 Exact Muffin-tin Orbitals

We solve the single-electron Equation (1.3) for the muffin-tin potential defined in Equation (2.1), by expanding the Kohn–Sham orbital $\Psi_j(\mathbf{r})$ in terms of *exact muffin-tin orbitals* $\bar{\psi}_{RL}^a(\epsilon_j, \mathbf{r}_R)$, *viz.*

$$\Psi_j(\mathbf{r}) = \sum_{RL} \bar{\psi}_{RL}^a(\epsilon_j, \mathbf{r}_R) v_{RL,j}^a. \quad (2.9)$$

The expansion coefficients, $v_{RL,j}^a$, are determined from the condition that the above expansion should be a solution for Equation (1.3) in the entire space. In the EMTO formalism, the algebraic formulation of this matching condition is the so called kink cancelation equation [46, 79, 80]. This equation is equivalent to the Korringa–Kohn–Rostoker tail cancelation equation [36, 37] written in a screened representation [38].

The exact muffin-tin orbitals form a complete basis set for the Kohn–Sham problem. They are defined for each lattice site R and for each $L \equiv (l, m)$, denoting the set of the orbital (l) and magnetic (m) quantum numbers. In practice, it is found that in Equation (2.9), the l summation can be truncated at $l_{max} = 3$, *i.e.* including the s, p, d and f muffin-tin orbitals only.

Screened Spherical Waves

The exact muffin-tin orbitals are constructed using different basis functions inside the potential spheres and in the interstitial region. In the interstitial region, where the potential is approximated by v_0 , we use as basis functions the solutions of the wave equation,

$$\left\{ \nabla^2 + \kappa^2 \right\} \psi_{RL}^a(\kappa^2, \mathbf{r}_R) = 0, \quad (2.10)$$

where $\kappa^2 \equiv \epsilon - v_0$, and ϵ is the energy. Within the EMTO formalism, the $\psi_{RL}^a(\kappa^2, \mathbf{r}_R)$ functions are referred to as the *screened spherical waves* [46].

The boundary conditions for Equation (2.10) are given in conjunction with non-overlapping spheres centered at lattice sites R with radii a_R . Although, the screening sphere radius might also depend upon the orbital quantum number l , for simplicity, here we assume that a_R depends only on the site index R . The screened spherical waves behave like a pure real harmonic $Y_L(\hat{r}_R)$ ³ on their own a -spheres, while the $Y_{L'}(\hat{r}_{R'})$ projections on all the other a -spheres, *i.e.* for $R' \neq R$, vanish [46]. With these energy independent boundary conditions, for κ^2 below the bottom of the a -spheres continuum, the screened spherical waves have short range and weak energy dependence [46, 79]. They form a complete basis set in the a -interstitial region and may be expanded in real harmonics $Y_{L'}(\hat{r}_{R'})$ around any site R' as

$$\begin{aligned} \psi_{RL}^a(\kappa^2, \mathbf{r}_R) &= f_{RL}^a(\kappa^2, r_R) Y_L(\hat{r}_R) \delta_{RR'} \delta_{LL'} \\ &+ \sum_{L'} g_{R'L'}^a(\kappa^2, r_{R'}) Y_{L'}(\hat{r}_{R'}) S_{R'L'RL}^a(\kappa^2). \end{aligned} \quad (2.11)$$

The expansion coefficients, $S_{R'L'RL}^a(\kappa^2)$, are the elements of the *slope matrix*, which is related to the well-known bare KKR structure constant matrix through an inhomogeneous Dyson equation [46]. This is introduced and discussed in Chapter 3.

In Equation (2.11), f_{RL}^a and g_{RL}^a are the value or head and the slope or tail functions, respectively. The previously described boundary conditions for the screened spherical waves for $l \leq l_{max}$ lead to the following conditions at the a -spheres

³ For the convention used for the real harmonics and for the Bessel and Neumann functions see Appendix B.

$$f_{RL}^a(\kappa^2, r)|_{a_R} = 1 \text{ and } g_{RL}^a(\kappa^2, r)|_{a_R} = 0. \quad (2.12)$$

Here we fix the slopes of f_{RL}^a and g_{RL}^a as⁴

$$\left. \frac{\partial f_{RL}^a(\kappa^2, r)}{\partial r} \right|_{a_R} = 0 \text{ and } \left. \frac{\partial g_{RL}^a(\kappa^2, r)}{\partial r} \right|_{a_R} = \frac{1}{a_R}. \quad (2.13)$$

Using the spherical Bessel and Neumann functions³, $j_l(\kappa^2, r_R)$ and $n_l(\kappa^2, r_R)$ respectively, the value and slope functions can be expressed as

$$f_{RL}^a(\kappa^2, r) = t_{RL}^1(\kappa^2)n_l(\kappa^2, r) + t_{RL}^2(\kappa^2)j_l(\kappa^2, r) \quad (2.14)$$

and

$$g_{RL}^a(\kappa^2, r) = -t_{RL}^3(\kappa^2)n_l(\kappa^2, r) - t_{RL}^4(\kappa^2)j_l(\kappa^2, r). \quad (2.15)$$

The coefficients $t_{RL}^{1, \dots, 4}$ are the screening parameters. They are chosen according to the imposed boundary conditions (2.12) and (2.13), namely

$$\begin{Bmatrix} t_{RL}^1(\kappa^2) & t_{RL}^2(\kappa^2) \\ t_{RL}^3(\kappa^2) & t_{RL}^4(\kappa^2) \end{Bmatrix} = 2 \frac{a_R^2}{w} \begin{Bmatrix} \frac{\partial j_l(\kappa^2, a_R)}{\partial r_R} & -\frac{\partial n_l(\kappa^2, a_R)}{\partial r_R} \\ \frac{1}{a_R} j_l(\kappa^2, a_R) & -\frac{1}{a_R} n_l(\kappa^2, a_R) \end{Bmatrix}. \quad (2.16)$$

Here w denotes the average atomic or Wigner–Seitz radius defined from the atomic volume V as

$$\frac{4\pi w^3}{3} \equiv V = \frac{\text{unit cell volume}}{\text{number of atoms in unit cell}}. \quad (2.17)$$

Since the Bessel and Neumann functions satisfy Equation (B.33), for the Wronskian of the value and slope functions we get

$$\mathcal{W}_r \{f_{RL}^a, g_{RL}^a\} = a_R, \quad (2.18)$$

and thus the determinant of the screening matrix becomes

$$d_{RL}^a \equiv t_{RL}^1(\kappa^2)t_{RL}^4(\kappa^2) - t_{RL}^2(\kappa^2)t_{RL}^3(\kappa^2) = -2 \frac{a_R}{w}. \quad (2.19)$$

According to Equations (2.11), (2.14) and (2.15), the screened spherical waves have no pure (lm) character⁵, and they are irregular at the origin. This problem is overcome in the next section by replacing the irregular head functions by the partial waves.

⁴ Different slopes at a -spheres can be used. For example, fixing the slope of g^a to $-1/a^2$ leads to a Hermitian slope matrix.

⁵ A function $f_L(\mathbf{r})$ has pure (lm) character if the angular part is fully described by a real harmonic, *viz.*, if $f_L(\mathbf{r}) = f_L(r) Y_L(\hat{r})$.

In Equation (2.11), $l \leq l_{max}$ and the l' summation is infinite. In practice, the latter is truncated at $l_{max}^h \approx 8 - 12$. For $l' > l_{max}$, the tail function reduces to the Bessel function, *i.e.* $g_{R'l'}^a(\kappa^2, r_{R'}) = -j_l(\kappa^2, r_{R'})$. These terms are called the *highers* and unlike the low- l components, they are allowed to penetrate into the a -spheres.

Partial Waves

Inside the potential sphere at R , the *partial waves* are chosen as the basis function. These are defined as the products of the regular solutions of the radial Schrödinger equation⁶ for the spherical potential $v_R(r_R)$,

$$\frac{\partial^2 \left[r_R \phi_{Rl}(\epsilon, r_R) \right]}{\partial r_R^2} = \left[\frac{l(l+1)}{r_R^2} + v_R(r_R) - \epsilon \right] r_R \phi_{Rl}(\epsilon, r_R), \quad (2.20)$$

and the real harmonics, *viz.*

$$\phi_{RL}^a(\epsilon, \mathbf{r}_R) = N_{RL}^a(\epsilon) \phi_{Rl}(\epsilon, r_R) Y_L(\hat{r}_R). \quad (2.21)$$

The normalization function $N_{RL}^a(\epsilon)$ should be determined from the matching conditions. The partial waves are defined for any real or complex energy ϵ and for $r_R \leq s_R$.

Because a screened spherical wave behaves like $Y_L(\hat{r}_R)$ only on its own a -sphere, the matching condition between $\psi_{RL}^a(\kappa^2, \mathbf{r}_R)$ and $\phi_{RL}^a(\epsilon, \mathbf{r}_R)$ should be set up at this sphere. On the other hand, as we have seen in Section 2.1.1, for an accurate representation of the single-electron potential the potential spheres should overlap. Therefore, usually we have $s_R > a_R$. Because of this, an additional free-electron solution with pure (lm) character has to be introduced. This function realizes the connection between the screened spherical wave at a_R and the partial wave at s_R . It joins continuously and differentiable to the partial wave at s_R and continuously to the screened spherical wave at a_R . Accordingly, the radial part of this backward extrapolated free-electron solution can be written in the form

$$\varphi_{RL}^a(\epsilon, r_R) = f_{RL}^a(\kappa^2, r_R) + g_{RL}^a(\kappa^2, r_R) D_{RL}^a(\epsilon), \quad (2.22)$$

where $D_{RL}^a(\epsilon) = \mathcal{D}\{\varphi_{RL}^a(\epsilon, a_R)\}$ is the logarithmic derivative of $\varphi_{RL}^a(\epsilon, r_R)$ calculated for $r_R = a_R$. By definition, the logarithmic derivative of a function $f(r_R)$ in the radial mesh point r_R^0 is

⁶ In practice, we solve the Dirac equation within the so called scalar relativistic approximation rather than the non-relativistic Schrödinger equation. This approximation is obtained by taking into account the mass-velocity and Darwin corrections and neglecting the spin-orbit interaction.

$$\mathcal{D}\{f(r_R^0)\} \equiv \frac{r_R^0}{f(r_R^0)} \frac{\partial f(r_R)}{\partial r_R} \Big|_{r_R=r_R^0}. \quad (2.23)$$

The normalization function in Equation (2.21) and the logarithmic derivative in Equation (2.22) are determined from the conditions

$$N_{RI}^a(\epsilon) \phi_{RI}(\epsilon, s_R) = \varphi_{RI}^a(\epsilon, s_R), \quad (2.24)$$

and

$$N_{RI}^a(\epsilon) \frac{\partial \phi_{RI}(\epsilon, r_R)}{\partial r_R} \Big|_{r_R=s_R} = \frac{\partial \varphi_{RI}^a(\epsilon, r_R)}{\partial r_R} \Big|_{r_R=s_R}, \quad (2.25)$$

After simple mathematics, we obtain

$$\frac{1}{N_{RI}^a(\epsilon)} = \frac{\phi_{RI}(\epsilon, s_R)}{f_{RI}^a(\kappa^2, s_R)} \frac{\mathcal{D}\{\phi_{RI}(\epsilon, s_R)\} - \mathcal{D}\{g_{RI}^a(\kappa^2, s_R)\}}{\mathcal{D}\{f_{RI}^a(\kappa^2, s_R)\} - \mathcal{D}\{g_{RI}^a(\kappa^2, s_R)\}}, \quad (2.26)$$

and

$$D_{RI}^a(\epsilon) = -\frac{f_{RI}^a(\kappa^2, s_R)}{g_{RI}^a(\kappa^2, s_R)} \frac{\mathcal{D}\{\phi_{RI}(\epsilon, s_R)\} - \mathcal{D}\{f_{RI}^a(\kappa^2, s_R)\}}{\mathcal{D}\{\phi_{RI}(\epsilon, s_R)\} - \mathcal{D}\{g_{RI}^a(\kappa^2, s_R)\}}. \quad (2.27)$$

In these expressions, $\mathcal{D}\{\phi_{RI}(\epsilon, s_R)\}$, $\mathcal{D}\{f_{RI}^a(\kappa^2, s_R)\}$ and $\mathcal{D}\{g_{RI}^a(\kappa^2, s_R)\}$ represent the logarithmic derivatives calculated according to Equation (2.23). Finally, the exact muffin-tin orbitals are constructed as the superposition of the screened spherical waves (2.11), the partial waves (2.21) and the free-electron solution (2.22), *viz.*

$$\begin{aligned} \bar{\psi}_{RL}^a(\epsilon, \mathbf{r}_R) &= \psi_{RL}^a(\kappa^2, \mathbf{r}_R) + N_{RI}^a(\epsilon) \phi_{RI}(\epsilon, r_R) Y_L(\hat{r}_R) \\ &\quad - \varphi_{RI}^a(\epsilon, r_R) Y_L(\hat{r}_R), \end{aligned} \quad (2.28)$$

where the last two terms are truncated outside the s -spheres.

2.1.3 Kink Cancellation Equation

With the exact muffin-tin orbitals defined in Equation (2.28), the trial wave function (2.9) around site R can be expressed as

$$\begin{aligned} \Psi(\mathbf{r}_R) &= \sum_L N_{RI}^a(\epsilon) \phi_{RI}(\epsilon, r_R) Y_L(\hat{r}_R) v_{RL}^a \\ &\quad + \sum_L \left[f_{RI}^a(\kappa^2, r_R) v_{RL}^a + g_{RI}^a(\kappa^2, r_R) \sum_{R'L'} S_{RLR'L'}^a(\kappa^2) v_{R'L'}^a \right] Y_L(\hat{r}_R) \\ &\quad - \sum_L [f_{RI}^a(\kappa^2, r_R) + g_{RI}^a(\kappa^2, r_R) D_{RI}^a(\epsilon)] Y_L(\hat{r}_R) v_{RL}^a. \end{aligned} \quad (2.29)$$

Here the index j has been omitted, emphasizing that the expansion may be written for any energy $\epsilon = \kappa^2 + v_0$. We observe that the head functions of the screened spherical wave (2.11) are canceled by the head functions of the free-electron solution (2.22). After rearranging the terms proportional to the tail function, we obtain

$$\begin{aligned} \Psi(\mathbf{r}_R) &= \sum_L N_{RL}^a(\epsilon) \phi_{RL}(\epsilon, r_R) Y_L(\hat{r}_R) v_{RL}^a + \sum_L g_{RL}^a(\kappa^2, r_R) Y_L(\hat{r}_R) \\ &\times \sum_{R'L'} [S_{RLR'L'}^a(\kappa^2) - \delta_{R'R} \delta_{L'L} D_{Rl}^a(\epsilon)] v_{R'L'}^a. \end{aligned} \quad (2.30)$$

This trial function will be a solution of Equation (1.3) for the muffin-tin potential (2.1), if inside the s -spheres the $l \leq l_{max}$ part of the second term from the right hand side of (2.30) vanishes for any r_R . That is, if the $l \leq l_{max}$ components of the screened spherical waves, multiplied by the expansion coefficients, are canceled exactly by $\varphi_{RL}^a(\epsilon, r_R) Y_L(\hat{r}_R) v_{RL,j}^a$. This is realized if the kink cancelation equation,

$$\sum_{RL} a_{R'} [S_{R'L'RL}^a(\kappa_j^2) - \delta_{R'R} \delta_{L'L} D_{Rl}^a(\epsilon_j)] v_{RL,j}^a = 0, \quad (2.31)$$

is satisfied for all R' and $l' \leq l_{max}$. Here and in the following $\kappa_j^2 \equiv \epsilon_j - v_0$, and ϵ_j is a Kohn–Sham single-electron energy for which Equation (2.31) has non-trivial solution. The difference between the slope matrix and the logarithmic derivative matrix is called the kink matrix,

$$K_{R'L'RL}^a(\epsilon_j) \equiv a_{R'} S_{R'L'RL}^a(\kappa_j^2) - \delta_{R'R} \delta_{L'L} a_R D_{Rl}^a(\epsilon_j). \quad (2.32)$$

Using the kink-cancelation equation, the wave function inside the potential sphere at R reduces to

$$\begin{aligned} \Psi_j(\mathbf{r}_R) &= \sum_L N_{RL}^a(\epsilon_j) \phi_{RL}(\epsilon_j, r_R) Y_L(\hat{r}_R) v_{RL,j}^a \\ &+ \sum_{L'}^{l' > l_{max}} g_{RL'}^a(\kappa_j^2, r_R) Y_{L'}(\hat{r}_R) \sum_{R'L} S_{RL'R'L}^a(\kappa_j^2) v_{R'L,j}^a. \end{aligned} \quad (2.33)$$

Note that the $l' > l_{max}$ components of $\psi_{RL}^a(\kappa_j^2, \mathbf{r}_R)$ are present in the potential spheres. However, due to the $l(l+1)/r_R^2$ centrifugal term in Equation (2.20), the partial waves for large l converge towards the Bessel functions, *i.e.* towards the second term from the right hand side of Equation (2.33).

The solutions of Equation (2.31) are the single-electron energies and wave functions. These solutions can be obtained from the poles of the path operator $g_{R'L'RL}^a(z)$ defined for a complex energy z by

$$\sum_{R''L''} K_{R'L'R''L''}^a(z) \bar{g}_{R''L''RL}^a(z) = \delta_{R'R} \delta_{L'L}. \quad (2.34)$$

In the case of translation symmetry, in Equations (2.31) and (2.34) the site indices run over the atoms in the primitive cell only, and the slope matrix, the kink matrix, and the path operator depend on the Bloch vector \mathbf{k} from the first Brillouin zone. The \mathbf{k} and energy dependent slope matrix is obtained from the Bloch sum

$$S_{Q'L'QL}^a(\kappa^2, \mathbf{k}) = \sum_T e^{i\mathbf{k}\mathbf{T}} S_{Q'L'(Q+\mathbf{T})L}^a(\kappa^2), \quad (2.35)$$

where Q' and Q denote two sites from the primitive cell, and \mathbf{T} is a translation vector.

2.1.4 Overlap Matrix

The overlap integral of the partial waves within the potential sphere of radius s_R is the norm of $\phi_{Rl}(\epsilon, r_R)$, *viz.*

$$\int \phi_{RL}^a *(\epsilon, \mathbf{r}_R) \phi_{RL}^a(\epsilon, \mathbf{r}_R) d\mathbf{r}_R = [N_{Rl}^a(\epsilon)]^2 \int_0^{s_R} \phi_{Rl}(\epsilon, r_R)^2 r_R^2 dr_R. \quad (2.36)$$

The radial integral can be calculated using the radial Schrödinger equation (2.20) and the Green's second theorem [46], and it gives

$$\int_0^{s_R} \phi_{Rl}(\epsilon, r_R)^2 r_R^2 dr_R = -s_R \dot{\mathcal{D}}\{\phi_{Rl}(\epsilon, s_R)\} \phi_{Rl}(\epsilon, s_R)^2, \quad (2.37)$$

where the over-dot denotes the energy derivative

$$\dot{\mathcal{D}}\{\phi_{Rl}(\epsilon, s_R)\} \equiv \frac{\partial \mathcal{D}\{\phi_{Rl}(\epsilon, s_R)\}}{\partial \epsilon}. \quad (2.38)$$

The corresponding expression for the free-electron solution (2.22) obtained between the s -sphere and a -sphere, is

$$\begin{aligned} \int_{a_R}^{s_R} \varphi_{Rl}^a(\epsilon, r_R)^2 r_R^2 dr_R &= \int_0^{s_R} \varphi_{Rl}^a(\epsilon, r_R)^2 r_R^2 dr_R - \int_0^{a_R} \varphi_{Rl}^a(\epsilon, r_R)^2 r_R^2 dr_R \\ &= -s_R \dot{\mathcal{D}}\{\varphi_{Rl}(\epsilon, s_R)\} \varphi_{Rl}^a(\epsilon, s_R)^2 + a_R \dot{\mathcal{D}}_{Rl}^a(\epsilon), \end{aligned} \quad (2.39)$$

where we have taken into account that $\varphi_{Rl}^a(\epsilon, a_R) = 1$. According to the matching conditions (2.24) and (2.25) we have

$$\mathcal{D}\{\varphi_{Rl}(\epsilon, s_R)\} = \mathcal{D}\{\phi_{Rl}(\epsilon, s_R)\} \quad (2.40)$$

for any ϵ , and thus

$$\dot{\mathcal{D}}\{\varphi_{Rl}(\epsilon, s_R)\} = \dot{\mathcal{D}}\{\phi_{Rl}(\epsilon, s_R)\}. \quad (2.41)$$

Therefore, the first term on the right hand side of Equation (2.39) is equal to the overlap integral of the partial waves (2.37).

The energy derivative of the logarithmic derivative function $\dot{D}_{Rl}^a(\epsilon)$ is calculated from Equation (2.27). The energy derivatives of the Bessel and Neumann functions, and their radial derivatives are obtained from the recurrence relations quoted in Appendix B, whereas $\dot{\mathcal{D}}\{\phi_{Rl}(\epsilon, s_R)\}$ is given in Equation (2.37).

The overlap integral of the screened spherical waves over the a -interstitial is obtained in a similar way using the wave equation (2.10) and Green's second theorem [46], and it has the following simple expression

$$\int_{\mathcal{I}^a} \psi_{R'L'}^{a*}(\kappa^2, \mathbf{r}_{R'}) \psi_{RL}^a(\kappa^2, \mathbf{r}_R) d\mathbf{r} = a_R \dot{S}_{R'L'RL}^a(\kappa^2), \quad (2.42)$$

where \mathcal{I}^a denotes a -interstitial. Here we recall that only the low- l components of $\psi_{RL}^a(\kappa, \mathbf{r}_R)$ are truncated outside the \mathcal{I}^a . The high- l components are present in the whole space, and their contribution to the overlap integral is included in Equation (2.42). The energy derivative of the slope matrix can be calculated from finite differences around κ^2 . Alternatively, one may use an analytic expression derived from the unscreened slope matrix. This will be presented in Section 3.1.

We can now establish the overlap matrix for the exact muffin-tin orbitals (2.28) calculated over the whole space. Let us assume, for the moment, that the potential spheres do not overlap and are smaller than the a -spheres. In this situation, we can split the integral $\int \bar{\psi}_{R'L'}^*(\epsilon, \mathbf{r}) \bar{\psi}_{RL}(\epsilon, \mathbf{r}) d\mathbf{r}$ into an integral of the partial waves over the potential sphere, an integral of the free-electron solutions over the region between the a -sphere and the potential sphere and an integral of the screened spherical waves over the a -interstitial. Using Equations (2.37), (2.39) and (2.42), we obtain

$$\begin{aligned} & \int \bar{\psi}_{R'L'}^*(\epsilon, \mathbf{r}) \bar{\psi}_{RL}(\epsilon, \mathbf{r}) d\mathbf{r} \\ &= a_R \dot{S}_{R'L'RL}^a(\kappa^2) - a_R \dot{D}_{Rl}^a(\epsilon) = \dot{K}_{R'L'RL}^a(\epsilon). \end{aligned} \quad (2.43)$$

For overlapping potential spheres, there are other small terms coming from the overlap region. However, these terms are small, and for reasonable small overlaps the above expression remains valid. For more details, the reader is referred to the work by Andersen and co-workers [46, 84].

2.1.5 The Fermi Level

During the iterations for solving self-consistently the Kohn–Sham equations (1.3), the Fermi energy ϵ_F is established from the condition that the total number of states $N(\epsilon_F)$ below the Fermi level should be equal to the number of electrons N_e from the system, *i.e.*

$$N(\epsilon_F) = N_e. \quad (2.44)$$

In practice, $N(\epsilon_F^*)$ is computed for a series of trial ϵ_F^* and the proper ϵ_F is obtained according to Equation (2.44).

Within the present method, we make use of the residue theorem (Appendix B) to find the number of states below the Fermi energy. According to this theorem, the contour integral of the properly normalized path operator gives the total number of states within the contour. Using the overlap matrix of the exact muffin-tin orbitals (2.43) to normalize the path operator, each electronic state will be normalized correctly within the real space. This leads to the following expression for the total number of states below the Fermi level:

$$N(\epsilon_F) = \frac{1}{2\pi i} \oint_{\epsilon_F} G(z) dz, \quad (2.45)$$

where

$$G(z) \equiv \sum_{R'L'RL} g_{R'L'RL}^a(z) \dot{K}_{RLR'L'}^a(z) - \sum_{RL} \left(\frac{\dot{D}_{Rl}^a(z)}{D_{Rl}^a(z)} - \sum_{\epsilon_{Rl}^D} \frac{1}{z - \epsilon_{Rl}^D} \right), \quad (2.46)$$

with $l, l' \leq l_{max}$. The energy integral in Equation (2.45) is performed on a complex contour that cuts the real axis below the bottom of the valence band and at ϵ_F . It is easy to see that near each pole ϵ_j , the path operator behaves like $\dot{K}_{RLR'L'}^a(\epsilon_j)/(z - \epsilon_j)$, and, therefore, the first term from the right hand side of Equation (2.46) will contribute with 1 to $N(\epsilon_F)$.

Because of the overlap matrix, the $g^a(z)\dot{K}^a(z)$ term may also include the poles of $\dot{D}^a(z)$. Here, we omit the R and l indices for simplicity. Let us denote by z_0 a pole of $\dot{D}^a(z)$. This pole has no physical meaning and should be removed from $N(\epsilon_F)$. Near z_0 , both $D^a(z)$ and $\dot{D}^a(z)$ diverge, and thus $g^a(z)\dot{K}^a(z) \rightarrow \dot{D}^a(z)/D^a(z)$ for $z \rightarrow z_0$. Therefore, subtracting $\dot{D}^a(z)/D^a(z)$ removes the nonphysical pole z_0 of $g^a(z)\dot{K}^a(z)$. In the second step, we have to restore the real poles of $\dot{D}^a(z)/D^a(z)$ due to the zeros of the logarithmic derivative function. We denote by ϵ^D a real energy where $D^a(z)$ vanishes. Expanding $D^a(z)$ near this energy, we have $D^a(z) \approx \dot{D}^a(\epsilon^D)(z - \epsilon^D) + \dots$, and thus $\dot{D}^a(z)/D^a(z) \approx 1/(z - \epsilon^D)$. Hence, $\dot{D}^a(z)/D^a(z) - 1/(z - \epsilon^D)$ contains

no poles due to the zeros of the logarithmic derivative function. Note that the second term from the right hand side of Equation (2.46) gives no contribution to $N(\epsilon_F)$ if $\dot{D}^a(z)$ is an analytic function of z inside the complex energy contour.

In Equation (2.43) the negligible terms due to the overlap between potential spheres have been omitted [84]. Besides these terms, $N(\epsilon_F)$ in Equation (2.45) gives the exact number of states at the Fermi level for the muffin-tin potential from Equation (2.1).

2.2 Electron Density

The electron density (1.7) is given in terms of Kohn–Sham single-electron wave functions. From the expansion of $\Psi_j(\mathbf{r})$ (Equation (2.9)), a multi-center form for the charge density can be obtained. Although, this multi-center expression gives a highly accurate charge density in the entire space, its application in the Poisson equation or the total energy functional is very cumbersome. Therefore, we seek a more transparent expression which can easily be used to compute the Hartree and exchange-correlation terms in Equations (1.4) and (1.9). To this end, we turn to the one-center expression (2.33). This expression is valid inside the potential spheres. Nevertheless, due to the kink-cancellation equation, the one-center expression remains valid for $r_R > s_R$ as well, if the normalized partial wave $N_{Rl}^a(\epsilon_j) \phi_{Rl}(\epsilon_j, r_R)$ is replaced by the backward extrapolated free-electron solution $\varphi_{Rl}^a(\epsilon_j, r_R)$. We use this expression to set up the one-center form for the charge density.

We divide the total density $n(\mathbf{r})$ into components $n_R(\mathbf{r}_R)$ defined inside the Wigner–Seitz cells,⁷ *viz.*

$$n(\mathbf{r}) = \sum_R n_R(\mathbf{r}_R). \quad (2.47)$$

Around each lattice site we expand the density components in terms of the real harmonics, *viz.*

$$n_R(\mathbf{r}_R) = \sum_L n_{RL}(r_R) Y_L(\hat{r}_R). \quad (2.48)$$

The partial components $n_{RL}(r_R)$ are radial functions, which are obtained using Equation (2.33), the residue theorem (Appendix B) and the orthogonality condition for the real harmonics (B.3). The final expression can be cast into the following form:

⁷ In practice, in order to be able to compute the density gradients and eventually the higher order density derivatives, the partial densities should in fact be defined inside a sphere which is slightly larger than the sphere circumscribed to the Wigner–Seitz cell.

$$n_{RL}(r_R) = \frac{1}{2\pi i} \oint_{\epsilon_F} \sum_{L''L'} C_{LL'L''} Z_{Rl''}^a(z, r_R) \times \tilde{g}_{RL''L'}^a(z) Z_{Rl'}^a(z, r_R) dz, \quad (2.49)$$

where $C_{LL'L''}$ are the real Gaunt numbers (Appendix B). For the radial functions the following notation has been introduced:

$$Z_{Rl}^a(z, r_R) = \begin{cases} N_{Rl}^a(z) \phi_{Rl}(z, r_R) & \text{if } l \leq l_{max} \text{ and } r_R \leq s_R \\ \varphi_{Rl}^a(z, r_R) & \text{if } l \leq l_{max} \text{ and } r_R > s_R \\ -j_l(\kappa r_R) & \text{if } l > l_{max} \text{ for all } r_R \end{cases}. \quad (2.50)$$

Note that in Equation (2.49), the l'' and l' summations include the *highers* as well, i.e. $l'', l' \leq l_{max}^h$. The low- l block of the generalized path operator $\tilde{g}_{RL'L}^a(z)$ is given by

$$\tilde{g}_{RL'L}^a(z) = g_{RL'RL}^a(z) + \frac{\delta_{L'L}}{a_R \dot{D}_{Rl}^a(z)} \left(\frac{\dot{D}_{Rl}^a(z)}{D_{Rl}^a(z)} - \sum_{\epsilon_{Rl}^D} \frac{1}{z - \epsilon_{Rl}^D} \right), \quad (2.51)$$

with $l, l' \leq l_{max}$. The second term from the right hand side of Equation (2.51) is introduced to remove the nonphysical poles of the normalization function $N_{Rl}^a(z)$. The off-diagonal blocks of $\tilde{g}_{RL'L}^a(z)$ are

$$\tilde{g}_{RL'L}^a = \begin{cases} \sum_{R''L''} g_{RL'R''L''}^a a_{R''} S_{R''L''RL}^a & \text{if } l' \leq l_{max}, l > l_{max} \\ \sum_{R''L''} S_{RL'R''L''}^a g_{R''L''RL}^a & \text{if } l' > l_{max}, l \leq l_{max} \end{cases}. \quad (2.52)$$

Finally, the high- l block is

$$\tilde{g}_{RL'L}^a = \sum_{R''L''R'''L'''} S_{RL'R''L''}^a g_{R''L''R'''L'''}^a a_{R'''} S_{R'''L'''RL}^a, \quad (2.53)$$

with $l', l > l_{max}$. For simplicity, in Equations (2.52) and (2.53), the energy dependence has been suppressed. The high-low and low-high blocks of the slope matrix are calculated by the blowing-up technique [83], which will be introduced in Chapter 3.

The charge density computed from Equations (2.48) and (2.49) is normalized within the unit cell, and for reasonably large l_{max}^h , it is continuous at the cell boundaries. Note that because the real Gaunt numbers vanish for $l > l'' + l'$, the partial components of the charge density are nonzero only for $l \leq 2l_{max}^h$. For a reasonably high l_{max}^h (10–12), however, the partial components with $l > l_{max}^h$ are very small. Because of this, the l -truncation in Equation (2.48) is usually set to l_{max}^h .

2.3 The Poisson Equation

Equations (2.31), (2.45) and (2.48) constitute the basis of the method used to solve the Schrödinger equation (1.3). In order to perform a self-consistent calculation, one constructs the electron density from the solutions of the kink cancelation equation and calculates the new effective single-electron potential. Within the EMTO formalism, this latter procedure involves two steps [47]. First, we calculate the full-potential from the total charge density (2.48), and second, we construct the optimized overlapping muffin-tin wells (2.1). Due to the l -truncation in the one-center expression from Equation (2.48), the first step is very demanding and inaccurate in the corners of the unit cell. Furthermore, the expression for the effective potential (1.4) involves an integral over the real space. These types of integrals can be performed using, *e.g.*, the shape function technique (Chapter 4). Applying this technique, however, would unnecessarily overcomplicate the self-consistent iterations. In the next section, we show that within the so called Spherical Cell Approximation [80], both of the above problems can be avoided.

2.3.1 Spherical Cell Approximation

To simplify the solution of the Poisson equation, during the self-consistent iterations, we substitute the Wigner–Seitz cell around each lattice site by a spherical cell. The volume of the spherical cell at R , Ω_{w_R} , may be chosen to be equal to the volume of the Wigner–Seitz cell Ω_R centered on the same lattice site, *i.e.*

$$\Omega_{w_R} \equiv \frac{4\pi}{3}w_R^3 = \Omega_R, \quad (2.54)$$

where w_R is the radius of the spherical cell.

Next, we investigate the overlapping muffin-tin approximation to the full-potential in the case of spherical cells. The integrated local deviation between the full-potential and the OOMT potential was introduced and discussed in Section 2.2. It represents a basic measure to establish the accuracy of the muffin-tin potential. But there are other important quantities which should be considered when searching for the best muffin-tin approximation.

The muffin-tin discontinuity is defined as the jump in the muffin-tin potential at the potential sphere boundary, $[v_R(s_R) - v_0]$. The error in the single-electron energies due to the overlap between the s -spheres is given as

$$\begin{aligned} \Delta E_{one} &\equiv \sum_{\epsilon_j \leq \epsilon_F} \Delta \epsilon_j \approx -\frac{\pi}{24} \sum_{RR'} |\mathbf{R} - \mathbf{R}'|^5 \omega_{RR'}^4 \\ &\times [v_R(s_R) - v_0][v_{R'}(s_{R'}) - v_0] n((\mathbf{R} - \mathbf{R}')/2). \end{aligned} \quad (2.55)$$

This expression has been obtained by the first order perturbation theory [42, 84]. Accordingly, ΔE_{one} is proportional to the average density within

the overlap region $n((\mathbf{R} - \mathbf{R}')/2)$, the square of the muffin-tin discontinuity, and the fourth order power of the linear overlap defined in Equation (2.7). Therefore, if we can keep the muffin-tin discontinuity small, the overlap errors will be negligible, and thus large overlapping potential spheres can be used.

Another important parameter is the constant potential from Equation (2.1) expressed relative to the Fermi level. The screened spherical waves have short range for energies below the bottom of the hard sphere continuum (Chapter 3). Therefore, in order to have localized slope matrices with a smooth energy dependence for energies below $\kappa^2 \approx \epsilon_F - v_0$, one prefers to have v_0 close to ϵ_F .

We make use again of the model potential (2.8) to illustrate how the above parameters depend on the potential sphere radius. For the integral in Equation (2.2) we consider two different domains: (A) the integral is carried out over the real Wigner–Seitz cells, and (B) the Wigner–Seitz cells are substituted by the spherical cells and the OOMT potential is derived for these cells, *i.e.* the integrals are performed within Ω_{w_R} .

In Figure 2.2, we show three sets of results for the integrated local deviation, the muffin-tin discontinuity and the constant potential. The first set (*a*, solid line) corresponds to the fully optimized overlapping muffin-tins calculated within the Wigner–Seitz cells (domain A). The second set (*b*, dotted line) is also obtained from the fully optimized overlapping muffin-tins, but this time they are calculated within the spherical cells rather than the Wigner–Seitz cell (domain B). The third case (*c*, dashed line) corresponds to partially optimized muffin-tins. In this case the spherical potential is fixed to the spherical part of the full-potential according to Equation (2.5) and for this $v(r)$ the constant potential v_0 is optimized within the domain B.

The integrated local deviations are plotted in the upper part of Figure 2.2. In contrast to the monotonously decreasing error obtained in case *a* (also shown in Figure 2.1), in the second case the error first decreases with s , at $\sim 15\%$ overlap it starts to increase and diverges at larger overlaps. In the third case, for overlapping s -spheres there is a moderate improvement of the muffin-tin approach relative to the non-overlapping situation, but above 30% overlap the integrated local deviation shows no significant dependence on the radius of the potential spheres.

The muffin-tin discontinuity is shown in the middle panel of Figure 2.2. With increasing overlap between the s -spheres, $[v(s) - v_0]$ converges smoothly to zero in case *a* and it diverges in case *b*. When v_0 is optimized for $v(r)$ fixed to the spherical part of the full-potential, $[v(s) - v_0]$ approaches zero at small overlaps and remains close to zero up to linear overlaps of 60–70%. Consequently, in the third case the single-electron energies of monoatomic systems are expected to depend negligibly on the overlap between the potential spheres [80].

The constant potential v_0 is plotted in the lower part of Figure 2.2. In case *a*, v_0 increases with s and reaches the zero potential level at $\sim 60\%$ overlap. When the muffin-tins are fully optimized inside the spherical cell, v_0 decreases

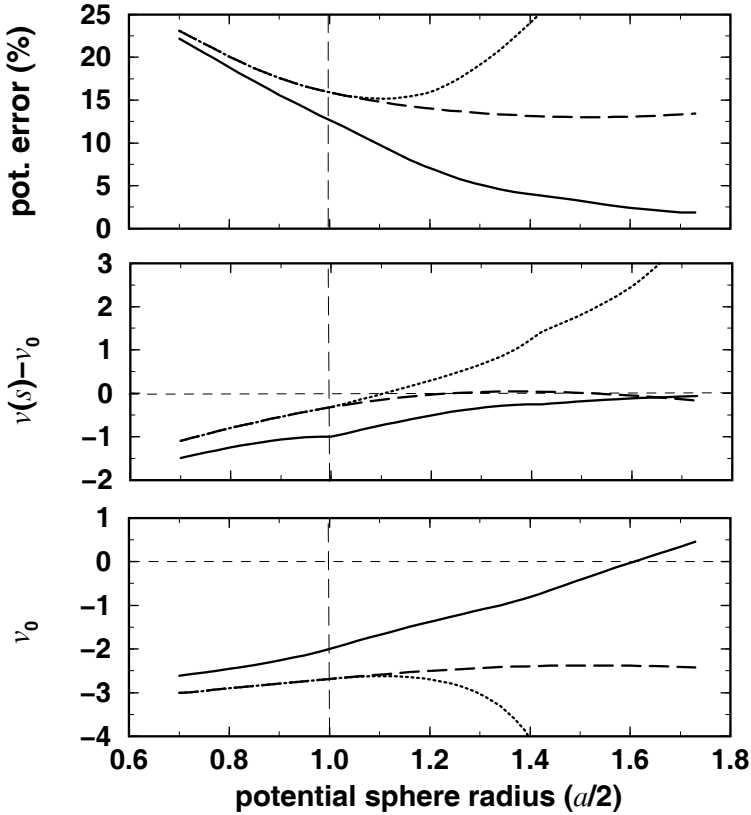


Fig. 2.2. Overlapping muffin-tin potential approximation to the cosine potential in a simple cubic lattice. Upper panel: integrated local deviation of the full-potential and overlapping muffin-tins (in %). Middle panel: muffin-tin discontinuity (in arbitrary units). Lower panel: muffin-tin zero (relative to the zero potential level, in arbitrary units). Solid line: fully optimized overlapping muffin-tins calculated in the Wigner–Seitz cells; dotted line: fully optimized overlapping muffin-tins calculated in the spherical cells; dashed line: spherical potential fixed to the spherical part of the full-potential and muffin-tin zero optimized for this spherical potential.

with s for overlaps larger than $\sim 15\%$. In the third case, v_0 increases slightly with the overlap but always remains well below its optimal value, *i.e.* the one from the first case.

From these results one clearly sees that using a spherical cell model, due to the improper description of the full-potential, the fully optimized overlapping muffin-tins approximation breaks down for linear overlaps larger than 10–15%. One possibility to overcome this problem is given by the third case (c), which we will refer to as the Spherical Cell Approximation (SCA).

In summary, the SCA involves two approximations. First, in Equation (2.2) the spherical cells rather than Wigner–Seitz cells are used, and second, $v_R(r_R)$ is fixed to the spherical average of the full-potential given in Equation (2.5). With this particular choice, the expression for parameter v_0 obtained from Equation (2.4) becomes [47, 80]

$$v_0 = \frac{\sum_R \int_{s_R}^{w_R} r_R^2 [\int v(\mathbf{r}) d\hat{\mathbf{r}}_R] dr_R}{\sum_R [4\pi(w_R^3 - s_R^3)/3]}. \quad (2.56)$$

When $s_R \rightarrow w_R$, the above expression reduces to

$$v_0 \rightarrow \frac{\sum_R [\int v(\mathbf{r}) d\hat{\mathbf{r}}_R]_{r_R=s_R} s_R^2}{\sum_R 4\pi s_R^2} = \frac{\sum_R v_R(s_R) s_R^2}{\sum_R s_R^2}. \quad (2.57)$$

One of the most important consequences of the SCA is that both $v_R(r_R)$ and v_0 from Equation (2.1) are given in terms of the spherical symmetric part of the full-potential, which can be computed efficiently and with high accuracy.

2.3.2 The Effective Potential

In this section, we establish an expression for the spherical part of the single-electron potential (1.4). An electron from a crystal feels the attractive potential (1.11) created by the nuclear charges located at the lattice sites R , and the repulsive electrostatic potential created by all the other electrons, *i.e.* the Hartree potential (1.5). Since both of these potentials have long range, they should be grouped in such a way that at large distance the negative and positive terms cancel each other. Usually, this is done by dividing $v_e(\mathbf{r}) + v_H(\mathbf{r})$ into components due to the charges from inside and from outside of the cell at R . The intra-cell part of the electrostatic potential then becomes

$$v_R^I(\mathbf{r}_R) = -\frac{2Z_R}{r_R} + 2 \int_{\Omega_R} \frac{n_R(\mathbf{r}'_R)}{|\mathbf{r}_R - \mathbf{r}'_R|} d\mathbf{r}'_R. \quad (2.58)$$

Using the expansion [87]

$$\frac{1}{|\mathbf{r}_R - \mathbf{r}'_R|} = 4\pi \sum_L \frac{1}{2l+1} \frac{r_R^l}{r_R'^{l+1}} Y_L(\hat{r}_R) Y_L(\hat{r}'_R), \quad (2.59)$$

valid for $r'_R > r_R$, we can separate the \mathbf{r}'_R integration in Equation (2.58). Calculating the spherical part of the resulting expression, we arrive at

$$\begin{aligned} v_R^I(r_R) &\equiv \frac{1}{4\pi} \int v_R^I(\mathbf{r}_R) d\hat{r}_R = 8\pi \frac{1}{r_R} \int_0^{r_R} r_R'^2 n_{RL_0}(r'_R) dr'_R \\ &+ 8\pi \int_{r_R}^{s_R} r'_R n_{RL_0}(r'_R) dr'_R - \frac{2Z_R}{r_R}, \end{aligned} \quad (2.60)$$

where $n_{RL_0}(r_R)$ is the $L_0 = (0, 0)$ partial component of the charge density near site R .

The effect of charges from outside of the potential sphere give the so called Madelung potential

$$v_R^M(\mathbf{r}_R) = - \sum_{R' \neq R} \frac{2 Z_{R'}}{|\mathbf{r}_{R'} + \mathbf{R}'|} + \sum_{R' \neq R} 2 \int_{\Omega_{R'}} \frac{n_{R'}(\mathbf{r}_{R'})}{|\mathbf{r}_R - \mathbf{r}_{R'} + \mathbf{R} - \mathbf{R}'|} d\mathbf{r}_{R'}. \quad (2.61)$$

This is calculated by expanding $\frac{1}{|\mathbf{r} - \mathbf{r}'|}$ first around $\mathbf{r}_R = \mathbf{r} - \mathbf{R}$ and then around $\mathbf{r}_{R'} = \mathbf{r}' - \mathbf{R}'$, namely

$$\frac{1}{|\mathbf{r} - \mathbf{r}'|} = 4\pi \sum_L \frac{1}{2l+1} \frac{r_R^l}{|\mathbf{r}' - \mathbf{R}'|^{l+1}} Y_L(\hat{r}_R) Y_L(\widehat{\mathbf{r}' - \mathbf{R}}), \quad (2.62)$$

and

$$\frac{Y_L(\widehat{\mathbf{r}' - \mathbf{R}})}{|\mathbf{r}' - \mathbf{R}'|^{l+1}} = \frac{4\pi}{(2l-1)!!} \sum_{L'L''} C_{LL'L''} \frac{(-1)^{l'} (2l''-1)!!}{(2l'+1)!!} \frac{r_{R'}^{l'}}{|\mathbf{R}' - \mathbf{R}|^{l''+1}} \times Y_{L'}(\hat{r}_{R'}) Y_{L'}(\widehat{\mathbf{R}' - \mathbf{R}}). \quad (2.63)$$

These expansions are strictly valid only for $r_R + r_{R'} < |\mathbf{R}' - \mathbf{R}|$, *i.e.* if the spheres circumscribed on the cells at R and R' do not overlap. The case of overlapping bounding spheres will be discussed in connection with the Madelung energy in Chapter 4. Using the above expressions, for the spherically symmetric part of the Madelung potential we obtain

$$v_R^M \equiv \frac{1}{4\pi} \int v_R^M(\mathbf{r}_R) d\hat{r}_R = \frac{1}{w} \sum_{R' \neq R, L'} M_{RL_0R'L'} Q_{R'L'}^{SCA}. \quad (2.64)$$

Here

$$M_{RL_0R'L'} = 8\pi (-1)^{l'} \sum_{L''} C_{LL'L''} \frac{(2l''-1)!!}{(2l-1)!! (2l'-1)!!} \delta_{l'', l'+l} \times \left(\frac{w}{|\mathbf{R}' - \mathbf{R}|} \right)^{l''+1} Y_{L''}(\widehat{\mathbf{R}' - \mathbf{R}}) \quad (2.65)$$

are the elements of the Madelung matrix, and w is the average atomic radius. Note that because of the Kronecker delta ($\delta_{l'', l'+l}$), in Equation (2.65) only

the $l'' = l' + l$ term is nonzero. The multipole moments, Q_{RL}^{SCA} , are calculated within the SCA,

$$Q_{RL}^{SCA} = \frac{\sqrt{4\pi}}{2l+1} \int_0^{w_R} \left(\frac{r_R}{w}\right)^l n_{RL}(r_R) r_R^2 dr_R - Z_R \delta_{L,L_0} + \delta^{SCA} \delta_{L,L_0}. \quad (2.66)$$

Since the integral in Equation (2.66) is performed over the spherical cell rather than over the unit cell, the monopole moments in Equation (2.66) have to be renormalized within the cell [80]. This is realized by the site independent constant δ^{SCA} , which is determined from the condition of charge neutrality, *viz.* $\sum_R Q_{RL_0}^{SCA} = 0$.

Usually, the number of electrons inside the s -sphere,

$$Q(s_R) = \frac{\sqrt{4\pi}}{2l+1} \int_0^{s_R} n_{RL}(r_R) r_R^2 dr_R, \quad (2.67)$$

is different from the number of electrons inside the cell, $Q_{RL_0}^{SCA} + Z_R$. This difference contributes a constant shift, Δv_R^M , to the spherical potential. In the SCA, this extra or missing charge is redistributed equally on the N_{NN} nearest-neighbor cells, *i.e.*

$$\Delta v_R^{SCA} = \frac{1}{w} \sum_{R_{NN}} M_{RL_0 R_{NN} L_0} \Delta Q_{R_{NN}}, \quad (2.68)$$

where $\Delta Q_{R_{NN}} \equiv \frac{1}{N_{NN}} (Q_{RL_0}^{SCA} + Z_R - Q(s_R))$ and R_{NN} are the nearest-neighbor sites.

Finally, the spherical symmetric part of the exchange-correlation potential (1.6) is

$$\mu_{xcR}(r_R) \equiv \frac{1}{4\pi} \int \mu_{xcR}([n_R]; \mathbf{r}_R) d\hat{r}_R. \quad (2.69)$$

The total potential within the potential sphere is obtained as the sum of contributions from Equations (2.60), (2.64), (2.68) and (2.69), namely

$$v_R(r_R) = v_R^I(r_R) + v_R^M + \Delta v_R^{SCA} + \mu_{xcR}(r_R). \quad (2.70)$$

Except the negligible approximations made in the Madelung terms, *i.e.* in Equations (2.64) and (2.68), the above expression gives the exact spherical part of the full potential inside the s -sphere.

In many application, the multipole moments in Equation (2.64) can be neglected for $l > 0$. Moreover, the non-spherical part of $\mu_{xcR}([n_R]; \mathbf{r}_R)$ from the right hand side of Equation (2.69), giving only a small contribution to the spherically symmetric exchange-correlation potential, can also be omitted. In this situation, all potential components in Equation (2.70) depend only on the

spherical symmetric density $n_{RL_0}(r_R)$. On the other hand, when the multipole moments for $l \neq 0$ are large (*e.g.*, near the free surfaces), the Madelung potential due to the higher order moments has to be taken into account. In this case, the l -truncation in Equation (2.64) is given by the l -truncation for the multipole moments, which in turn is l_{max}^h used for the charge density (see Section 2.2). In practice, however, the l -truncation for the charge density during the self-consistent iterations can be set to a value (usually 4–6) smaller than the one used to calculate the final full charge density, without sacrificing the accuracy of the method.

Before closing this section, we shall comment on the numerical calculation of the Madelung potential for a periodic bulk (infinite) system. When collecting different contributions to v_R^M , the R' summation in Equation (2.64) should run over all the lattice sites. The Madelung matrix (2.65) can easily be computed for any pair of lattice points R and R' . However, since $M_{RL_0R'L'} \sim 1/|\mathbf{R} - \mathbf{R}'|^{l'+1}$, for the low order multipole moments ($l' \leq 1$), the R' summation diverges. This is because at large distance the number of sites included in the Madelung sum roughly increases as the surface of the coordination shell, *i.e.* as $4\pi|\mathbf{R} - \mathbf{R}'|^2$. On the other hand, the unit cells are neutral, and thus the contribution coming from a remote cell should vanish. In order to overcome this problem, the lattice summation should be carried out using the so called Ewald technique. For details about this technique, the reader is referred to Skriver [39].

2.3.3 Potential Sphere Radius s_R

The potential sphere radius influences the accuracy of the muffin-tin approximation. In Section 2.3.1, we saw that in the case of monoatomic systems the integrated local deviation between full-potential and OOMT potential decreases and the constant potential is pushed towards the Fermi level with increasing potential sphere radius. But what is even more important, large potential spheres also lead to decreased muffin-tin discontinuity and thus to decreased error coming from the s -sphere overlap. On the other hand, this error is proportional to the fourth order power of the linear overlap between spheres [42, 84], which sets an upper limit for s_R .

In Figure 2.3, the overlap error and the muffin-tin discontinuity (inset) are plotted as a function of the potential sphere radius in the case of face centered cubic (*fcc*) Cu. These calculations were done at the experimental volume using the SCA. We find that for linear overlaps between $\sim 4\%$ and $\sim 20\%$ the muffin-tin discontinuity is below 10 mRy. This results in a negligible error in the single-electron energies. On the other hand, at larger overlaps the error diverges rapidly with increasing s_R . Taking into account that the integrated local deviation shows a weak s_R dependence for overlaps above $\sim 10\%$ (see Figure 2.2), we conclude that in close-packed monoatomic systems the best representation of the full-potential within SCA can be achieved by choosing potential spheres with a linear overlap between 10% and $\sim 25\%$.

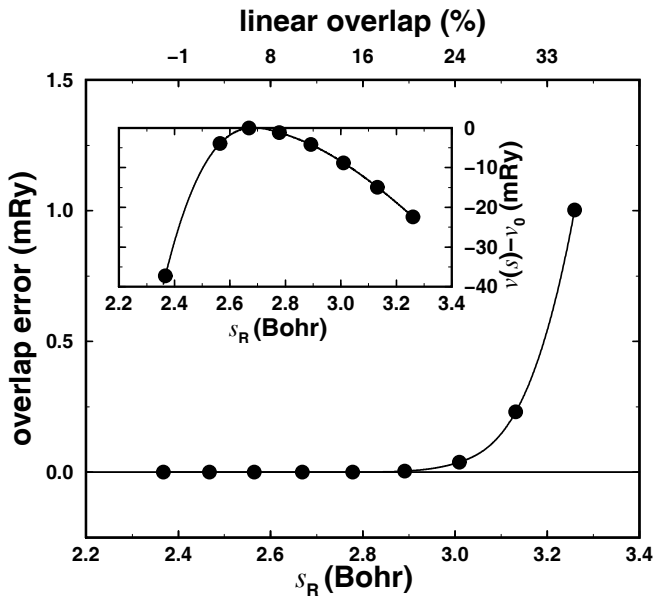


Fig. 2.3. The overlap error for face centered cubic Cu ($w = 2.669$ Bohr) as a function of the potential sphere radius. In the inset the muffin-tin discontinuity is plotted.

In a polyatomic system, small muffin-tin discontinuity can be obtained if the individual spherical potentials at the potential sphere boundary have similar values, *i.e.*

$$v_R(s_R) \approx v_{const.} \quad \text{for each } R. \quad (2.71)$$

Then the constant potential, obtained as the average of the spherical potentials calculated in the vicinity of s_R , will be $v_0 \approx v_{const.}$ and therefore $v_R(s_R) - v_0 \approx 0$. For well localized slope matrices, $v_{const.}$ from Equation (2.71) should have the maximum possible value.

The effect of s_R on the muffin-tin discontinuity in polyatomic crystals is illustrated in the case of magnesium diboride. The crystal structure of MgB_2 has the hexagonal symmetry (space group $P6/mmm$) with $a = 5.833$ Bohr and $c/a = 1.14$ [88, 89, 90]. Layers of Mg and B atoms are located at $z = 0$ and $z = 0.5c/a$, respectively. Using $s_R = w_R$ corresponding to $s_{\text{Mg}}/s_{\text{B}} \approx 1.12$, the linear overlap between nearest-neighbor B atoms is 42%. In this situation, the actual value of the muffin-tin discontinuity is crucial for an accurate self-consistent calculation. In Figure 2.4, we plotted the two muffin-tin discontinuities $[v_{\text{Mg}}(s_{\text{Mg}}) - v_0]$ and $[v_{\text{B}}(s_{\text{B}}) - v_0]$ calculated around Mg and B sites, respectively. Different symbols correspond to different pairs of s_{Mg} and s_{B} . For example, triangles represent muffin-tin discontinuities $+0.288$

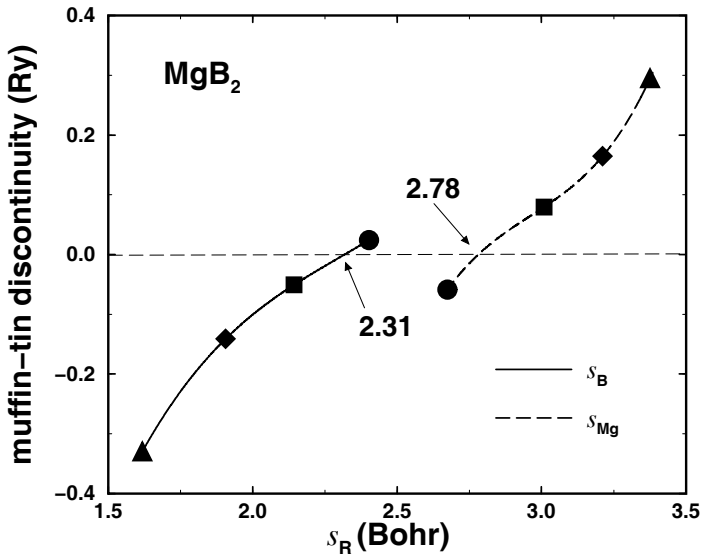


Fig. 2.4. The two muffin-tin discontinuities in MgB_2 compound as functions of the Mg and B potential sphere radii.

Ry and -0.335 Ry obtained using $s_{Mg} = 3.37$ Bohr and $s_B = 1.62$ Bohr. We can see that there is a particular ratio, namely $s_{Mg}/s_B \approx 1.26$, when the muffin-tin discontinuity vanishes on both sites. Although the linear overlap between boron sites is still around 30%, with this choice for s_{Mg} and s_B the error in the single-electron energies is found to be negligible.



<http://www.springer.com/978-1-84628-950-7>

Computational Quantum Mechanics for Materials

Engineers

The EMT0 Method and Applications

Vitos, L.

2007, XII, 237 p. 92 illus., Hardcover

ISBN: 978-1-84628-950-7